

See discussions, stats, and author profiles for this publication at: <https://www.researchgate.net/publication/230567131>

# Self-Assembled Plasmonic Vesicles of SERS-Encoded Amphiphilic Gold Nanoparticles for Cancer Cell Targeting and Traceable Intracellular Drug Delivery

ARTICLE in JOURNAL OF THE AMERICAN CHEMICAL SOCIETY · JULY 2012

Impact Factor: 12.11 · DOI: 10.1021/ja305154a · Source: PubMed

---

CITATIONS

104

---

READS

38

3 AUTHORS, INCLUDING:



Jibin Song

National Institute of Biomedical Imaging and ...

19 PUBLICATIONS 515 CITATIONS

SEE PROFILE



Jiajing Zhou

Nanyang Technological University

11 PUBLICATIONS 332 CITATIONS

SEE PROFILE

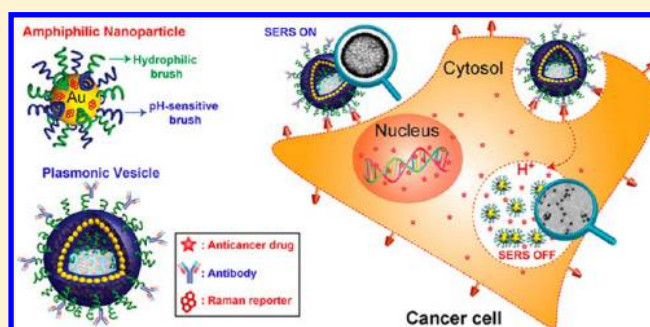
# Self-Assembled Plasmonic Vesicles of SERS-Encoded Amphiphilic Gold Nanoparticles for Cancer Cell Targeting and Traceable Intracellular Drug Delivery

Jibin Song, Jiajing Zhou, and Hongwei Duan\*

School of Chemical and Biomedical Engineering, Nanyang Technological University, 70 Nanyang Drive, Singapore 637457

## S Supporting Information

**ABSTRACT:** We report the development of bioconjugated plasmonic vesicles assembled from SERS-encoded amphiphilic gold nanoparticles for cancer-targeted drug delivery. This new type of plasmonic assemblies with a hollow cavity can play multifunctional roles as delivery carriers for anticancer drugs and SERS-active plasmonic imaging probes to specifically label targeted cancer cells and monitor intracellular drug delivery. We have shown that the pH-responsive disassembly of the plasmonic vesicle, stimulated by the hydrophobic-to-hydrophilic transition of the hydrophobic brushes in acidic intracellular compartments, allows for triggered intracellular drug release. Because self-assembled plasmonic vesicles exhibit significantly different plasmonic properties and greatly enhanced SERS intensity in comparison with single gold nanoparticles due to strong interparticle plasmonic coupling, disassembly of the vesicles in endocytic compartments leads to dramatic changes in scattering properties and SERS signals, which can serve as independent feedback mechanisms to signal cargo release from the vesicles. The unique structural and optical properties of the plasmonic vesicle have made it a promising platform for targeted combination therapy and theranostic applications by taking advantage of recent advances in gold nanostructure based in vivo bioimaging and photothermal therapy and their loading capacity for both hydrophilic (nucleic acids and proteins) and hydrophobic (small molecules) therapeutic agents.



## INTRODUCTION

Plasmonic metal nanoparticles with localized surface plasmon resonance (LSPR) arising from the collective excitation of conduction electrons have found widespread use in biosensing, bioimaging, surface-enhanced spectroscopy, and drug delivery.<sup>1,2</sup> The LSPR wavelength of plasmonic nanoparticles is broadly tunable across the visible and near-infrared spectral range by controlling their structural parameters (size, shape, and chemical composition) and local environment (the refractive index of surrounding medium and interparticle distances of nearby nanoparticles).<sup>1,3</sup> In particular, LSPR spectral shifts induced by interparticle plasmonic coupling have attracted considerable research interest in controlled assembly of plasmonic nanoparticles, which, in conjugation with responsive “smart” coatings, has been exploited to detect a wide range of molecular targets and environmental factors in bulk assays.<sup>1,4–6</sup> Interestingly, the strong light scattering of plasmonic nanoparticles at their LSPR wavelengths also offers the possibility to develop miniature single-particle sensors, detectable by scattering-based plasmonic imaging.<sup>1a,7–9</sup> Discrete assemblies of plasmonic nanoparticles with biologically tailorable interparticle spacing have served as “molecular rulers” for real-time optical tracking of the dynamic interaction of biomolecules in vitro and in live cells.<sup>8,9</sup> On the other hand, recent advances in plasmonics, especially the reproducible

synthesis of well-defined plasmonic nanostructures, have stimulated considerable research efforts in surface-enhanced Raman scattering (SERS), which is emerging as a powerful tool for spectroscopic detection of molecular, cellular, and in vivo targets.<sup>2b,10</sup> Enhancement factors up to  $10^{14}$ – $10^{15}$  can be achieved by properly adjusting the LSPR wavelength and structural features of the nanoparticles, the adsorption site and spectroscopic profile of Raman probes, and the excitation wavelength.<sup>10,11</sup> Accumulating evidence has proved that interparticle plasmonic coupling in nanoparticle assemblies affords an enhanced electromagnetic field in the interstitial spaces, which can significantly amplify the SERS signal of Raman probes coated on the nanoparticle surface, thus making it possible to detect the surface-coating-mediated assembly/disassembly of SERS-encoded nanoparticles using Raman spectroscopy.<sup>12,13</sup>

Here we report the development of plasmonic vesicles assembled from SERS-active amphiphilic gold nanoparticles for cancer-targeted drug delivery, which can be tracked by plasmonic imaging and Raman spectroscopy. Both gold nanoparticles,<sup>14–16</sup> with excellent biocompatibility, unique physicochemical properties, and well-defined surface chemistry,

Received: May 28, 2012

Published: July 25, 2012

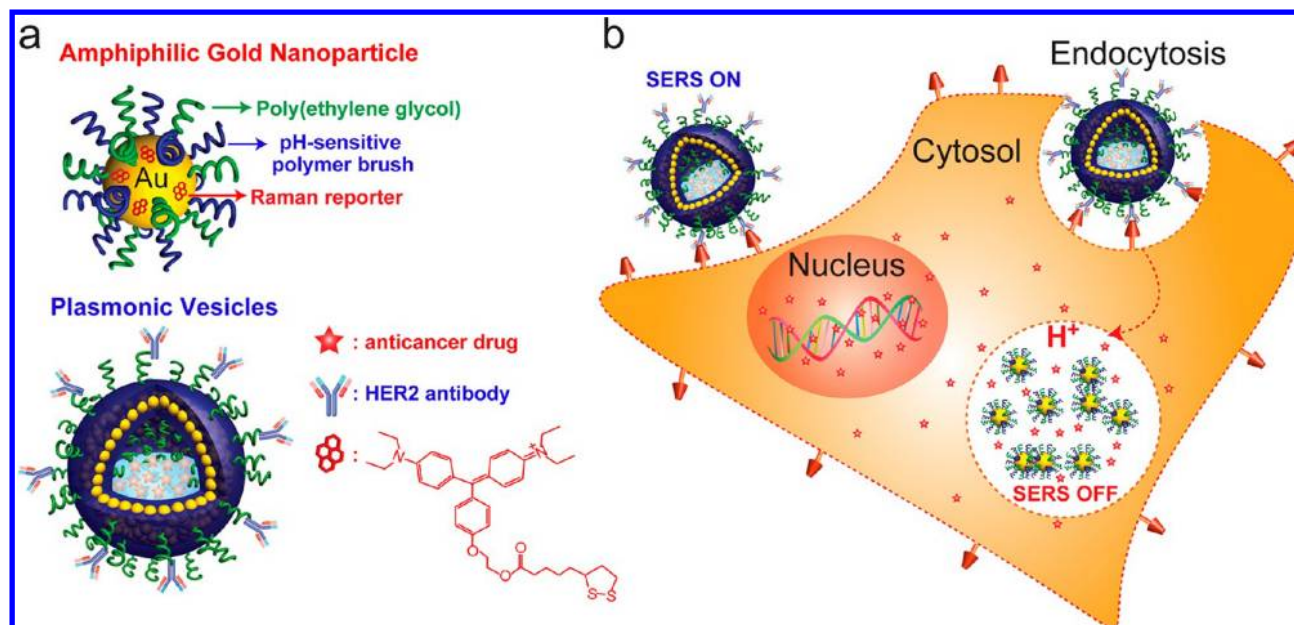


**Figure 1.** (a) Schematic illustration of the amphiphilic gold nanoparticle coated with Raman reporter BGLA and mixed polymer brushes of hydrophilic PEG and pH-sensitive hydrophobic PMMAVP grafts and the drug-loaded plasmonic vesicle tagged with HER2 antibody for cancer cell targeting. (b) The cellular binding, uptake, and intraorganelle disruption of the SERS-encoded pH-sensitive plasmonic vesicles.

and polymeric vesicles (also known as polymersomes),<sup>17,18</sup> with robust structures and versatile chemical functionality, are intriguing drug delivery carriers under intense research. Our recent research has demonstrated that amphiphilic nanoparticles carrying mixed polymer brush coatings with distinctly different hydrophobicity can self-assemble into vesicles with the functional nanoparticles embedded in the shell formed by the hydrophobic brushes and the hydrophilic brushes extending into aqueous environment to stabilize the structures, as illustrated in Figure 1.<sup>19</sup> Earlier research on amphiphilicity driven self-assembly of polymer-grafted gold nanoparticles has focused on the structural and optical properties of the resultant discrete assemblies.<sup>19,20</sup> The use of these plasmonic assemblies in biological environment remains largely unexplored. One key finding in this study is that this new type of plasmonic assemblies with a hollow cavity can play multifunctional roles as delivery carriers for anticancer drugs and plasmonic imaging probes to specifically label targeted cancer cells, when tagged with cancer-targeting ligands. More interestingly, pH-responsive disassembly of the plasmonic vesicle, stimulated by the hydrophobic-to-hydrophilic transition of the hydrophobic brushes in acidic intracellular compartments, allows for triggered intracellular drug release, which can be monitored in real-time by both plasmonic imaging and Raman spectroscopy.

There is growing interest in theranostic nanomedicine with integrated imaging and therapeutic modalities for simultaneous diagnosis, disease treatment, and monitoring of therapeutic efficacy.<sup>21</sup> Additional functionalities such as stimuli-triggered payload release and feedback mechanisms on the releasing process are highly desirable. Payload release in response to external stimuli such as pH provides the opportunity to take advantage of disease-specific physiological conditions, such as acidic extracellular environment of solid tumors and acidic intracellular endocytic compartments for localized therapy.<sup>22</sup> Delivery carriers with built-in optical or spectroscopic schemes to signal the release kinetics are of particular importance for

better understanding on the releasing mechanism/kinetics and high-throughput screening of drug candidates.<sup>23</sup> Currently, feedback on payload release from carriers primarily relies on the change of fluorescence resonance energy transfer (FRET) efficiency between the carriers and the payloads, when their binding falls apart.<sup>23</sup> Since efficient FRET occurs only when the donor–acceptor pair has necessary spectral overlapping in their emission and excitation profiles, this strategy is only applicable for a small group of optically active therapeutic agents.<sup>24</sup> In this study, we have shown that self-assembled plasmonic vesicles exhibit significantly different plasmonic properties and greatly enhanced SERS intensity in comparison with single gold nanoparticles, resulting from strong interparticle plasmonic coupling. Consequently, intracellular disassembly of the vesicles in endocytic compartments leads to dramatic changes in scattering properties and SERS signals, which, unlike FRET, can serve as independent feedback mechanisms to signal cargo release from the vesicles. The light scattering of plasmonic nanoparticles is free of photobleaching and photoblinking commonly observed in fluorescent probes such as small molecular dyes and semiconductor quantum dots,<sup>8</sup> therefore offering unique advantages for continuous tracking of the intracellular drug delivery. Recent progress in bioimaging have shown that gold nanoparticles are promising contrast agents for in vivo imaging techniques such as photoacoustic imaging and optical coherence tomography,<sup>25</sup> which, along with the successful use of SERS probes for solid tumor detection,<sup>26</sup> implies the potential in vivo applications of plasmonic vesicles as a versatile theranostic platform.

## RESULTS AND DISCUSSION

**Self-Assembly and pH-Triggered Destruction of Plasmonic Vesicles.** To synthesize the SERS-active amphiphilic nanoparticles, citrate-stabilized gold nanoparticles 14 nm in size were first coated with a Raman reporter. Afterward, the mixed polymer brushes of hydrophilic poly(ethylene glycol) (PEG) and hydrophobic copolymer (PMMAVP) of methyl



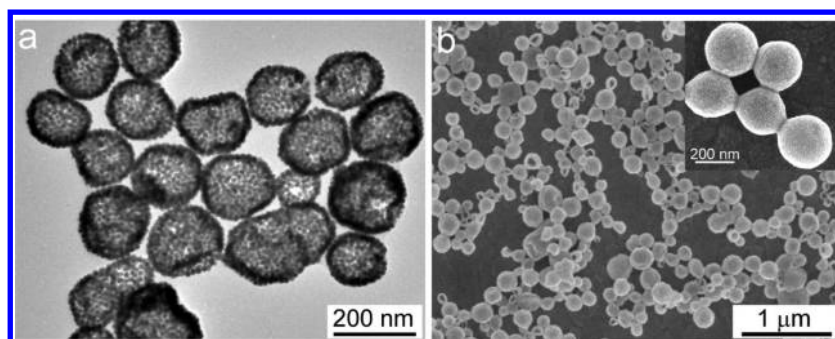


**Figure 2.** TEM (a) and SEM (b) images of the pH-sensitive plasmonic vesicles assembled from 14 nm gold nanoparticles with mixed PEG and PMMAVP brushes.

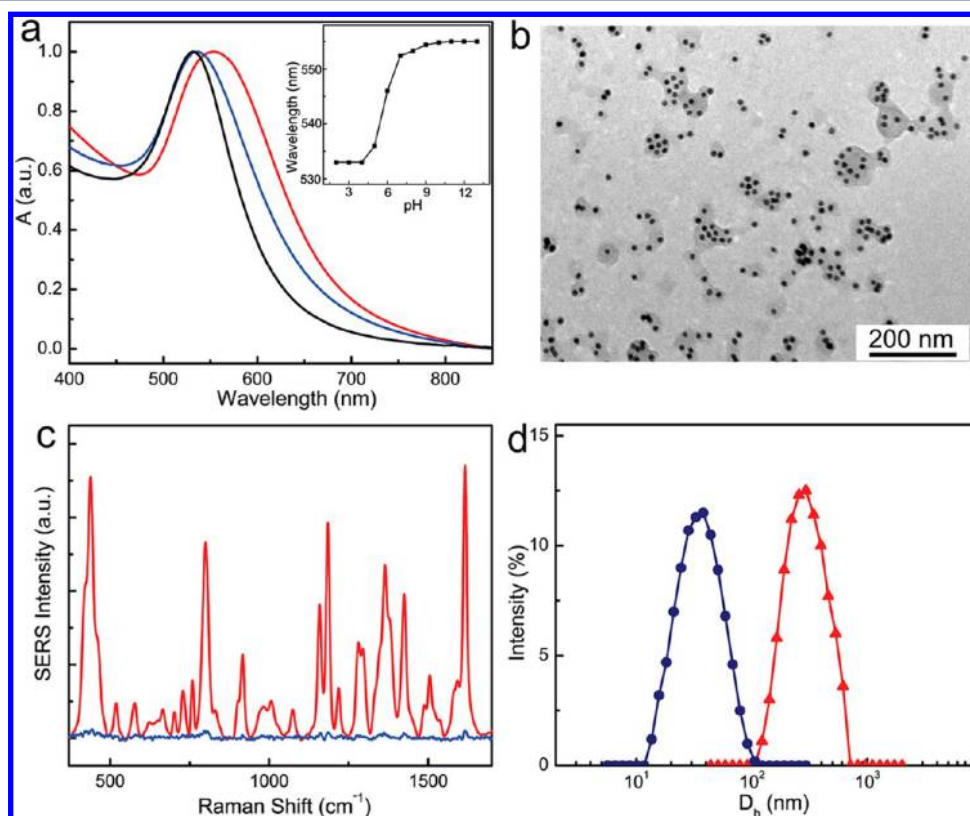


**Figure 3.** (a) UV-vis spectra of the amphiphilic gold nanoparticles and the vesicles: gold nanoparticles in chloroform (black solid line), vesicles at pH 7.4 (red line), and the disassembled vesicles at pH 5.0 (blue line). (Inset: LSPR peak wavelength of the vesicles as a function of solution pH). (b) TEM image of the disassembled vesicle at pH 5.0. (c) Raman spectra of the vesicle at pH 7.4 (red) and pH 5.0 (blue). (d) Hydrodynamic diameter distribution of the vesicles at pH 7.4 (red) and pH 5.0 (blue).

methacrylate (MMA) and 4-vinylpyridine (4VP) were grafted on the gold nanoparticles using the tandem “grafting to” and “grafting from” strategy that we developed recently.<sup>19,27</sup> In the grafting to step, thiolated PEG and 2,2'-dithiobis[1-(2-bromo-2-methylpropionyloxy)]ethane (DTBE), an atom transfer radical polymerization (ATRP) initiator with a disulfide group, were attached on gold nanoparticles by forming covalent Au–S bonds. In the following grafting from step, the PMMAVP brushes were grown on the functionalized nanoparticles through surface-initiated ATRP. The resultant amphiphilic nanoparticles on average have 82 PEG ( $M_n = 5$  kDa) grafts and 164 PMMAVP ( $M_n = 24$  kDa) grafts based on a PEG:PMMAVP molar ratio of 1:2 and a grafting density of  $0.4 \text{ chain/nm}^2$ , which is obtained from the molecular weights and the weight fraction (21%) of the polymer brushes

measured by thermogravimetric analysis (see the Supporting Information for details). Previous reports by several groups have shown that Raman molecules nonspecifically adsorbed on gold nanoparticles were not displaced by polymeric ligands such as thiolated PEG during ligand exchange reactions.<sup>26</sup> In this work, we have found that the small molecular ligand DTBE can effectively remove the weakly bound Raman molecules such as crystal violet because of the formation of the more favorable Au–S bond. In contrast, the Raman dye BGLA<sup>27b</sup> with a brilliant green backbone and a multivalent disulfide anchoring group (Figure 1) can survive over the ligand exchange reaction with PEG and DTBE and therefore was selected as the Raman tag of the amphiphilic gold nanoparticles. The dense layer of hydrophilic brushes covering the self-assembled plasmonic vesicles (Figure 1) is expected to play

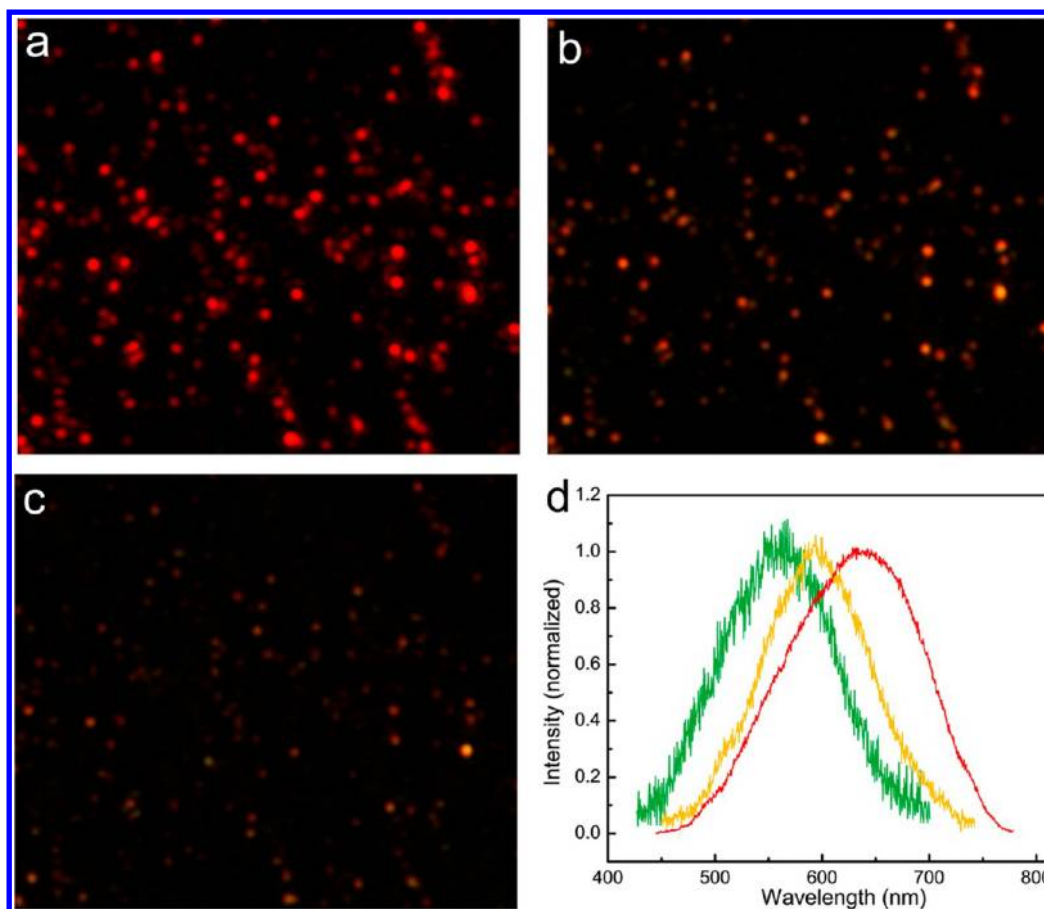


**Figure 4.** (a–c) Dark-field images of the pH-sensitive vesicles show the scattering color change upon the addition of pH 5.0 HCl. (d) Representative scattering spectra of the vesicle reveal the corresponding spectral shifts.

a dominant role in the surface properties and colloidal stability of the vesicles. We have used PEG as the hydrophilic brush because the highly flexible and hydrated PEG chain has shown the capability to improve the biocompatibility, colloidal stability, and blood circulation of nanoparticles in biological environment.<sup>26,28</sup> Note that 35% of the thiolated PEG chains were heterofunctional PEG with a carboxylic acid terminal group, which can be used for chemical conjugation of cancer-targeting ligands. The 4VP moiety ( $\sim 10\%$ ) in the hydrophobic PMMAVP brush has a  $pK_a$  of 5.4,<sup>29</sup> below which the copolymer becomes water-soluble due to the protonation of pyridine groups. This hydrophobic-to-hydrophilic transition at pH 5.4 is of particular interest for the stimulated disruption of plasmonic vesicles in intracellular acidic compartments such as late endosomes/lysosomes (pH  $\sim 4.7$ – $5.5$ ).<sup>30</sup> The ability of gold nanoparticles to amplify SERS signal is size-dependent, and single nanoparticles smaller than 20 nm are not efficient SERS substrates.<sup>31</sup> With the use of 14 nm nanoparticle as the building block of plasmonic vesicles, we aim to minimize the background signal from individual gold nanoparticles and achieve a greater signal contrast between the assembled vesicles and single particles.

The amphiphilic gold nanoparticles were assembled into vesicles via the film rehydration method commonly used for preparing polymersomes of amphiphilic block copolymers.<sup>32</sup> The TEM image (Figure 2a) of the vesicles shows spherical ensembles of closely attached nanoparticles with a clear contrast between the interior and the periphery, which is characteristic for hollow structures with a large cavity. The shell

thickness of the vesicle about 200 nm in diameter is less than 20 nm, indicating that a monolayer of amphiphilic nanoparticles is present on the vesicle shell, in which the hydrophobic PMMAVP brushes collapse to form the shell matrix with nanoparticle embedded and the hydrophilic PEG chains extend to cover the exterior and interior surfaces, as depicted in Figure 1. SEM observation (Figure 2b) confirms the vesicular structure with a hollow cavity, and the densely packed nanoparticles on the vesicle surface became clearly visible at higher magnification. The dense packing of gold nanoparticles led to strong interparticle plasmonic coupling, which is evidenced by the 25 nm red-shift (Figure 3a) of the LSPR peak relative to that (531 nm) of the single nanoparticles in chloroform. The vesicles have shown excellent colloidal stability in neutral or basic buffer solutions. Although they settled to the bottom of the storage vial in a week, which is commonly observed for heavy gold colloids, a homogeneous dispersion can be readily recovered with gentle shaking for a few seconds. The LSPR peak, SERS spectrum, and hydrodynamic size of the vesicle remained unchanged for at least 3 months at 25 °C. Upon tuning the pH from 7.4 to 5.0, which is expected to induce the dissolution of the hydrophobic PMMAVP brushes, the LSPR peak blue-shifted by 20 nm, suggesting an increase in the interparticle spacing. In TEM images (Figure 3b), single nanoparticles or small clusters rather than intact vesicles were observed, confirming the pH-triggered destruction of the plasmonic vesicles. The interparticle coupling has led to plasmonic vesicles with strong SERS activity, which shows an ensemble-averaged enhancement factor of  $7.2 \times 10^4$ .

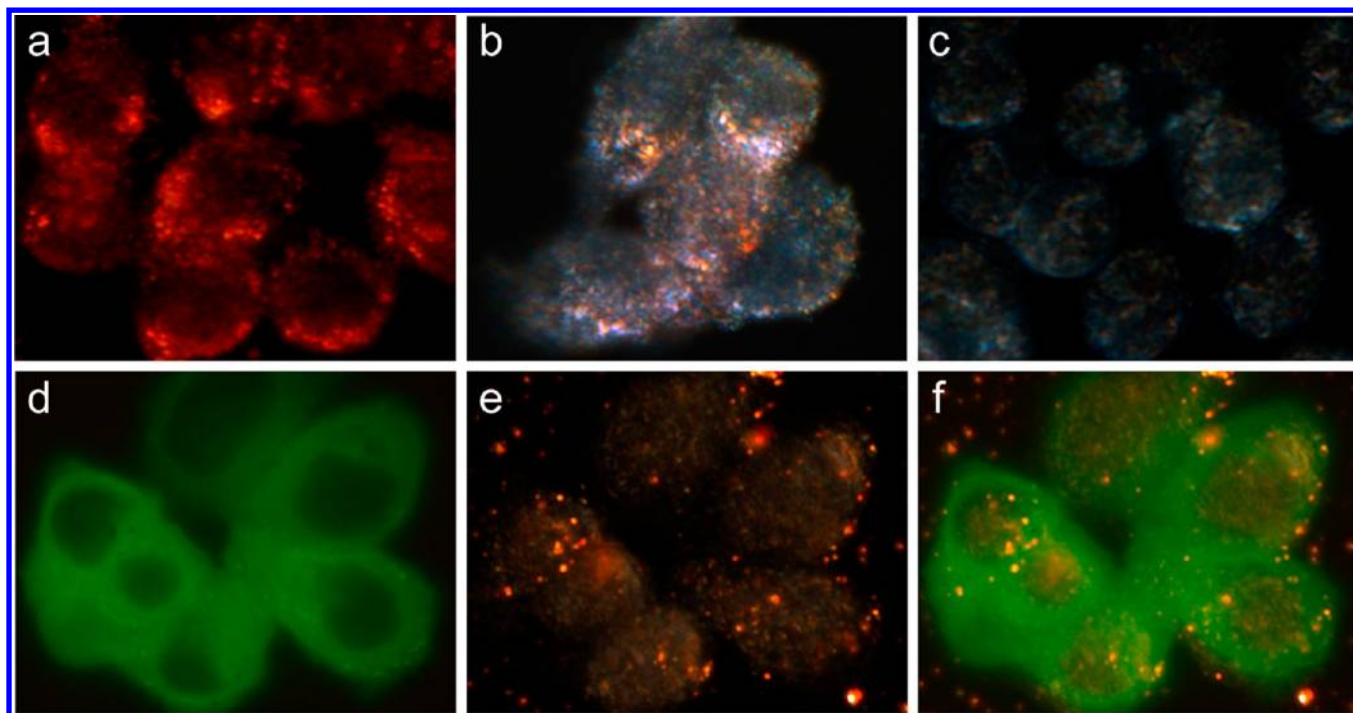


**Figure 5.** Dark-field images of live SKBR-3 cells incubated with HER2-targeted vesicles (a), nontargeted vesicles (b), and cell culture medium only (c). Fluorescence (d), dark-field (e), and the overlaid images of the MCF-7 cells with GFP stably expressed on their tubulin.

The dissociation of plasmonic vesicles also can be followed by the change of SERS intensity, and as shown in Figure 3c, the strong fingerprint SERS signal of the vesicle dropped dramatically by 34-fold at  $1615\text{ cm}^{-1}$  and became very weak upon the pH change. Dynamic light scattering measurements (Figure 3d) also revealed that the plasmonic vesicles with a hydrodynamic size of  $\sim 255\text{ nm}$  fall apart into smaller objects  $27\text{ nm}$  in size.

We have also used single-particle imaging to track the vesicle dissociation. Scattering color and spectra of the vesicles immobilized on a glass substrate of a flow chamber were monitored under a dark-field microscope with a colored CCD camera and a spectrometer. Light scattering intensity of plasmonic structures is sensitive to the size of the nanoparticles and the interparticle spacing in ensembles of nanoparticles. Plasmonic coupling between nanoparticles leads to spectral redshifts of the scattering light (that is, a color change in the visible spectral region) and greater scattering cross sections in comparison with that of single particles.<sup>1a,8</sup> As a result, although  $14\text{ nm}$  gold nanoparticle used here has negligible light scattering, the plasmonic vesicles exhibit intense red-colored scattering due to the strong interparticle coupling (Figure 4). Once pH 5.0 HCl solution was added into the flow chamber to trigger the vesicle disruption, scattering from individual vesicles showed a color change from red to yellow even greenish yellow with decreasing intensities. In line with this observation, gradual spectral blue-shifts in the scattering spectra (Figure 4d) of single vesicles were detected due to the increase of interparticle spacing caused by the electrostatic repulsion of protonated polymer chains and the dissolution of nanoparticles into the aqueous medium. The photobleaching-free light scattering of plasmonic nanoparticles at their LSPR wavelengths has made them promising imaging labels. These results suggest that it is possible to utilize the well-defined vesicular assemblies of gold nanoparticles with a built-in sensing

mechanism in the hydrophobic brushes for real-time monitoring of local environment.

**Cancer Cell Targeting and the Intracellular Disassembly of the Plasmonic Vesicles.** To test the cancer cell targeting properties of the plasmonic vesicles, we have conjugated the vesicles with a monoclonal antibody to HER2 protein, which is overexpressed on many types of breast cancer cells and has become a biomarker for diagnosis and target of therapy.<sup>33</sup> Figure 5 shows that the bioconjugated vesicles quickly bound to HER2-positive SKBR-3 breast cancer cells (see Supporting Information, Figure S4) after incubating for 30 min. The entirety of cells was labeled with a large number of vesicles and became red in color under dark-field microscope, as compared with control cells exhibiting low background scattering. We note that incubation of the vesicles with SKBR-3 cells for up to 90 min led to time-dependent cell labeling, and 30 min of incubation was sufficient to afford strong plasmonic signals on the cells (see Supporting Information, Figure S5), which is supportive of the efficient receptor-mediated cellular uptake of the vesicles. Also in clear contrast is that pegylated vesicles without targeting ligands only led to a low level of labeling due to nonspecific binding. To further confirm that the cellular binding and uptake is a HER2-specific event, HER2-negative MCF-7 breast cancer cells<sup>34</sup> (see Supporting Information, Figure S4) with green fluorescent protein (GFP) stably expressed on their tubulin were used as a control cell. The combined fluorescence and dark-field imaging (Figure 5d–f) revealed sparsely distributed vesicles on MCF-7 cells. These results collectively demonstrate the potential of using bioconjugated plasmonic vesicles to recognize and label specific types of cancer cells. The vesicles are expected to be uptaken by the cells through the endocytic pathway. The strong scattering of the vesicles allows continuous imaging of their intracellular behavior. The punctuated distribution of vesicles indicates that they were trapped inside intracellular compartments, which was



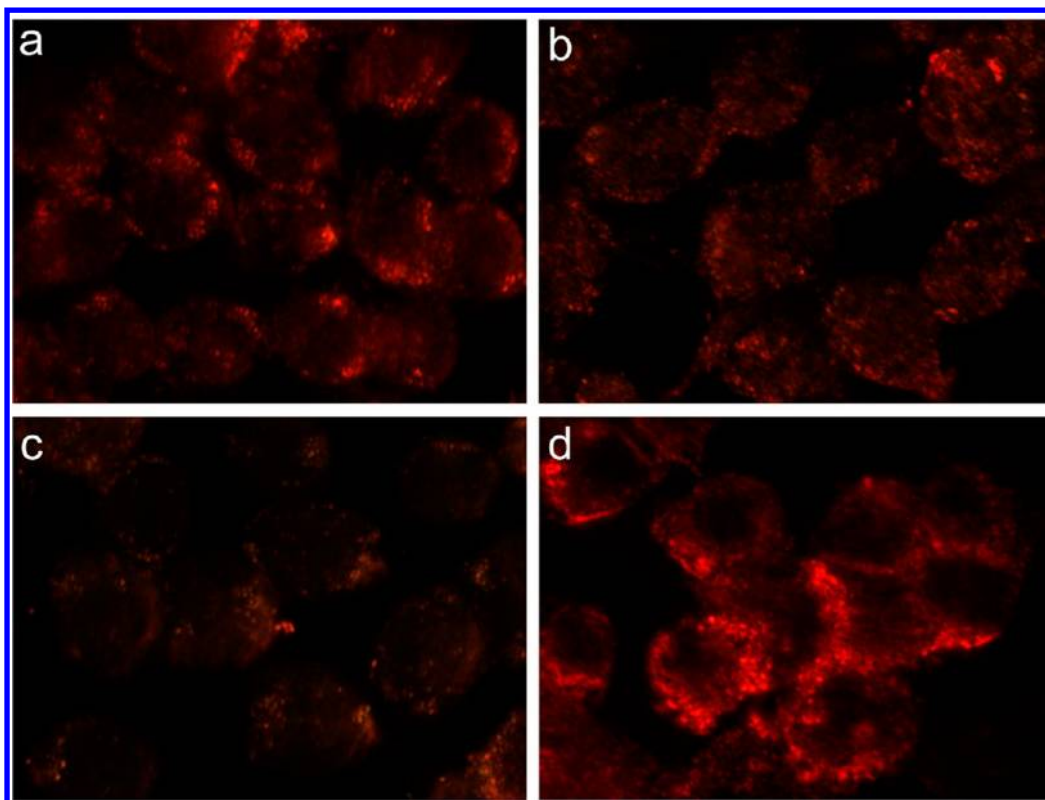


**Figure 6.** Dark-field images of SKBR-3 cells incubated with targeted pH-sensitive vesicles for 30 min (a) and the postincubation images of the cells at 60 min (b) and 90 min (c). (d) Dark-field image of SKBR-3 cells labeled with pH-insensitive vesicles, taken at 2 h after 30 min incubation.

further confirmed by the colocalization of the vesicles with organelles stained with green fluorescent 3,3'-dioctadecyloxycarbocyanine perchlorate (DiO) (see the Supporting Information, Figure S6).<sup>35</sup> It was observed that the scattering of internalized plasmonic vesicles had both color changes from orange-red to green-yellow and intensity drop within 1 h (Figure 6a–c), which should result from the dissociation of the vesicles when the organelles evolved from early endosomes (pH 5.9–6.2) to late endosomes/lysosomes (pH 4.7–5.5).<sup>30</sup> The fact that pH-insensitive vesicles of gold nanoparticles with PEG and PMMA brushes internalized into SKBR-3 cells did not show any color changes in 2 h (Figure 6d) further confirmed that it is indeed the acidification of organelles that stimulated the disruption of the vesicles inside the endocytic organelles.

Raman spectroscopy results (Figure 7) showed similar trends in cell targeting and intracellular disintegration of the vesicles, as observed in plasmonic imaging. While the vesicle-labeled SKBR-3 cells displayed the strong fingerprint Raman signal of the BGLA probe, significantly weaker Raman signals were detected from the SKBR-3 cells exposed to nontargeted vesicles and MCF-7 cells incubated with targeted vesicles. In agreement with the results of plasmonic imaging, the SKBR-3 cells labeled with pH-sensitive vesicles also showed gradually reduced SERS intensity in the same timeline. Consistent efforts have been made in developing sensors and imaging probes to detect extracellular or intracellular pH because of the interest in taking advantage of physiological conditions to facilitate cargo release and elucidating the intracellular processing of internalized objects.<sup>36,37</sup> Plasmonic nanoparticles and assemblies encoded with pH-sensitive Raman reporters recently have been used to monitor local pH changes in live cells.<sup>37</sup> For example, 4-

mercaptobenzoic acid with relatively simple and pH-sensitive spectral profiles in the pH range of 4–8 has become the Raman reporter of choice for measuring intracellular pH variations.<sup>37</sup> Our plasmonic vesicles with covalently linked pH-sensitive polymer brushes provide opportunities to utilize plasmonic coupling for dual-modality (dark-field imaging and Raman spectroscopy) detection. Particularly, we have demonstrated that it is possible to achieve cell-selective sensing using targeting ligand conjugated vesicles.

**Drug Loading/Release and Traceable Intracellular Drug Delivery.** We next investigated the use of plasmonic vesicles for loading and pH-triggered release of anticancer drugs. Doxorubicin (DOX), a first-line chemotherapy for breast cancer, was selected as the model drug for this proof-of-concept study. A number of approaches toward efficient loading of DOX into the well-studied vesicular drug carriers such as liposomes and polymersomes have been developed by taking advantage of the pH-dependent solubility of DOX ( $pK_a \sim 8.3$ ).<sup>38,39</sup> For instance, creating a pH gradient across the vesicular membrane can drive the accumulation of DOX inside the acidic aqueous cavity of liposomes and polymersomes.<sup>38</sup> We have devised a modified film-rehydration method to prepare DOX-loaded plasmonic vesicles. DOX deprotonated with equal molar of triethylamine was dissolved in chloroform and codeposited with the amphiphilic gold nanoparticles to form the film for rehydration with pH 7.4 PBS or pH 10  $\text{NaHCO}_3$  buffer. The loading content of DOX continuously rose when the feeding weight ratios of DOX and the vesicles were increased up to 40%, as shown in Figure 8a. This is reasonable because increasing the amount of DOX available for loading is expected to result in higher loading content. Meanwhile, we have found that the use of pH 7.4 PBS for

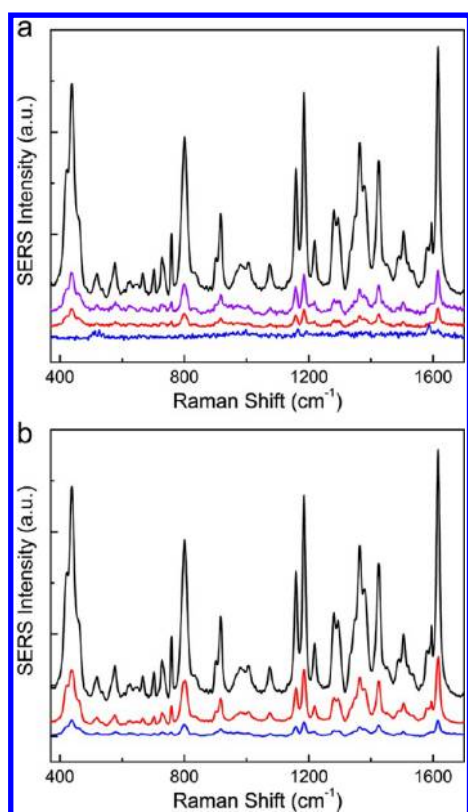


**Figure 7.** (a) Representative SERS spectra of SKBR-3 cells treated with HER2-targeted vesicles (black line) and untargeted vesicle (purple line), MCF-7 cells treated with targeted vesicles (red line), and SKBR-3 control cells (blue line). (b) Representative SERS spectra of SKBR-3 cells labeled with targeted vesicles after 30 min incubation (black line) and the postincubation spectra of the cells at 60 min (red line) and 90 min (blue line).

vesicle preparation consistently led to loading efficiencies about 10% lower than the experiments performed at pH 10, and the highest loading efficiency of 71% was obtained at the DOX feeding weight ratio of 25% at pH 10 (Figure 8b). Since the addition of DOX of more than 30% of the vesicle weight for encapsulation gave rise to plasmonic vesicles with poor stability, we have fixed the feeding of DOX at 25% for the release and cellular experiments. Similar to liposomes and polymersomes, the plasmonic vesicles also offer both aqueous cavity to hold hydrophilic payloads and hydrophobic membrane to trap hydrophobic compounds. We reason that the higher loading efficiency of the DOX at pH 10 benefits from the efficient entrapment of the insoluble DOX molecules in the hydrophobic shell of the plasmonic vesicles. In contrast, at pH 7.4, water-soluble DOX had a tendency to partition into the aqueous medium, leading to DOX partially encapsulated in the aqueous cavity, whereas those leaked into the exterior environment would be lost. Lecommandoux and co-workers<sup>39</sup> recently have shown that the deprotonated DOX at pH 10.5 formed aggregates in the hydrophobic membrane of polymersomes, and at pH 7.4, DOX was primarily encapsulated in the aqueous cavity.

To further elucidate the encapsulation mechanism, the fluorescence spectra (Figure 8c) of the samples obtained at different pH values were measured. Considering that DOX is unstable at basic conditions and the spectral properties of DOX are dependent on its protonation state, the DOX-loaded vesicles prepared at pH 10 were purified by centrifugation and

redispersed in pH 7.4 PBS immediately after preparation. Notably, DOX loaded at pH 10 recovered its optical properties at pH 7.4 after the purification. Our results showed that the fluorescence intensity of the same amount of DOX loaded at pH 7.4 is 3 times stronger than that of DOX loaded at pH 10, and DOX in plasmonic vesicles exhibited considerably lower fluorescence intensity than free DOX. Gold nanoparticles are excellent quenchers for fluorescence molecules in their close proximity.<sup>24</sup> The lower fluorescence intensity of the sample prepared at pH 10 is likely caused by both the fluorescence quenching of membrane-entrapped DOX by gold nanoparticles on the vesicle shell and self-quenching due to the aggregation of DOX, whereas, for the DOX-loaded vesicle obtained at pH 7.4, the fluorescence emission of DOX in the aqueous cavity can be absorbed by the gold nanoparticles, leading to the lower fluorescence than that of the free DOX. The similar quenching effect of the gold nanoparticles for DOX in the shell should also play an important role. Overall, the DOX in the cavity that experiences reduced quenching by gold nanoparticles led to the stronger fluorescence of the vesicles prepared at pH 7.4.

The drug release profile (Figure 8d) of the plasmonic vesicles also showed strong pH-dependence. Both pH-sensitive Au@PEG/PMMAVP vesicles at pH 7.4 and pH-insensitive Au@PEG/PMMA vesicles at pH 5.0 showed minimal drug release over 24 h, suggesting the stable encapsulation of DOX by the vesicles. In contrast, the Au@PEG/PMMAVP vesicles at pH 5.0 quickly released 80% of the encapsulated DOX within 30 min. It is believed that both the immediate disruption of plasmonic vesicles and higher water-solubility of DOX at pH 5.0 contributed to the pulsatile drug release. Importantly, the dramatic changes in scattering property and SERS intensity of the plasmonic vesicles and the drug release occur in response to the same pH trigger, which is highly relevant to the acidic environment of endocytic compartments. This fact suggests that it is possible to use plasmonic imaging and Raman spectroscopy to monitor the drug release from the endocytosed vesicles.

Figure 9 displays the dual-modality imaging of the DOX-loaded plasmonic vesicles in live SKBR-3 cells. The strong fluorescence of DOX at 590 nm and the light scattering of the plasmonic vesicles allows for independently tracking the cargo and carriers using fluorescence and dark-field imaging, respectively. The cell nuclei were counterstained with Hoechst 3342 exhibiting blue fluorescence. The sample prepared at pH 7.4 was used in the cellular imaging because of its stronger fluorescence. The integrated results of dark-field and fluorescence imaging clearly revealed three distinct stages in terms of the cellular binding and intracellular distribution of plasmonic vesicles and DOX molecules. The drug-loaded vesicles first recognized the cells, directed by the conjugated HER2 antibodies, and primarily accumulated at the cell membrane region after incubating with the cells for 30 min. At this stage, signals from DOX and plasmonic vesicles were highly colocalized, suggesting that DOX was still retained in the vesicles. Both of the scattering and fluorescence imaging showed evident changes 30 min later. The scattering color of the plasmonic vesicles changed from orange-red to orange-yellow, which corresponds to a decreased interparticle plasmonic coupling and an increase in interparticle spacing. The fluorescence of DOX was not colocalized with the vesicles and strong signal appeared in the cytosol, indicating that DOX was released from the vesicles into the cytoplasm. The patched pattern of the scattering signal implies that the dissociated gold



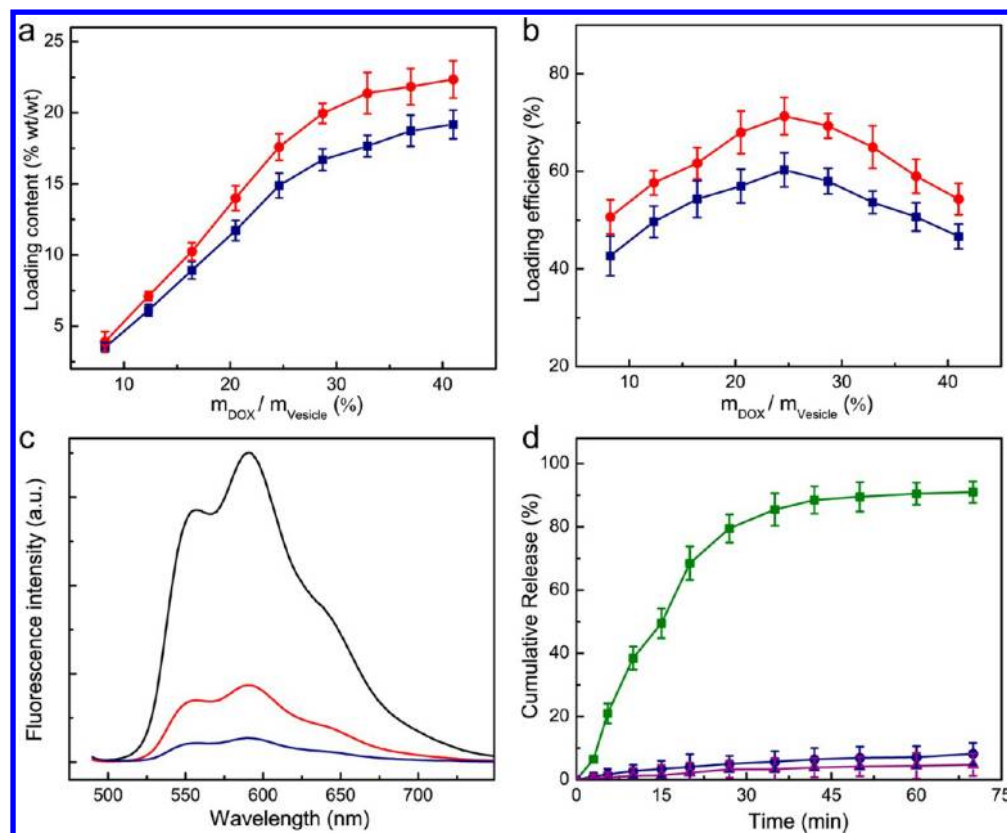


**Figure 8.** DOX loading content (a) and loading efficiency (b) in the pH-sensitive vesicles at pH 7.4 (blue line) and pH 10 (red line) as a function of the feeding weight ratio of DOX to the vesicles. (c) Fluorescence spectra of free DOX (black line) and DOX-loaded vesicles prepared at pH 7.4 (red line) and pH 10 (blue line) at the same DOX concentration. (d) In vitro release profiles of DOX-loaded pH-sensitive vesicles at pH 5.0 (green line) and pH 7.4 (blue line) and DOX-loaded pH-insensitive vesicle at pH 5.0 (purple line).

nanoparticles were trapped inside the endocytic compartments. At the third stage, DOX fluorescence became mainly overlapped with that of the nuclei, indicating that the DOX molecules penetrated into the nuclei and bound to their targets; the scattering color of the vesicle further changed from orange-yellow to green-yellow. Consistent with the plasmonic imaging results, the disruption of plasmonic vesicles was triggered when the surrounding pH gradually changed from physiological pH (7.4) to acidic pH in early endosomes (pH 5.9–6.2) and late endosomes/lysosomes (pH 4.7–5.5), and this process can be monitored by the alteration of the scattering color. More importantly, our results have shown that the scattering signal variation can be correlated with the DOX release profile. Since the increase of interparticle spacing in the vesicles has immediate impact on the membrane permeability of the vesicles and the releasing kinetics of the payload encapsulated, the change of scattering signal can be used as a direct feedback mechanism to signal the cargo release from the plasmonic vesicles. This becomes more important for the general use of plasmonic vesicles to track the intracellular delivery of optically inactive therapeutic agents. Notably, the DOX-loaded vesicles maintained the cell selectivity of the antibody-conjugated vesicles, showing a low-level of cellular uptake on MCF-7 cells (see Supporting Information, Figure S7). Furthermore, the targeted plasmonic vesicles showed no adverse effect on the proliferation of SKBR-3 cells (Figure 10), indicative of the biocompatibility of the plasmonic vesicles. When the targeted vesicles were loaded with DOX, they became highly toxic to the cells, with an estimated half maximal inhibitory concentration

( $IC_{50}$ ) of  $0.31 \mu\text{g/mL}$ , which is about 5-fold lower than that of the nontargeted vesicles. This result is in line with the poor cellular uptake of the nontargeted vesicles (Figure 5b). Consistent with the minimal drug release from the integral vesicles shown above (Figure 8d), the targeted pH-insensitive vesicles of gold nanoparticles coated with PEG and PMMA grafts did not lead to obvious cell toxicity, further verifying that the effective cancer cell killing by the targeted pH-sensitive vesicles is a result of pH-triggered DOX release.

## CONCLUSION

We have developed a new class of bioconjugated plasmonic vesicles assembled from SERS-encoded gold nanoparticles with mixed amphiphilic polymer brush coating for cancer-targeted drug delivery. The strong interparticle plasmonic coupling gives rise to plasmonic vesicles with significantly different plasmonic properties and greatly enhanced SERS intensity in comparison with single gold nanoparticles. Using pH-sensitive plasmonic vesicles for stimulated intracellular drug release in acidic endocytic organelles, we have demonstrated that this multi-functional drug carrier not only allows for efficient cargo loading and release but also can generate independent optical and spectroscopic feedback on the cargo release by plasmonic imaging and SERS spectroscopy. The development of gold nanoparticle based contrast agents for in vivo imaging techniques such as photoacoustic imaging and optical coherence tomography and the successful use of SERS probes for solid tumor detection strongly imply the in vivo applications of plasmonic vesicles as a versatile theranostic platform. We

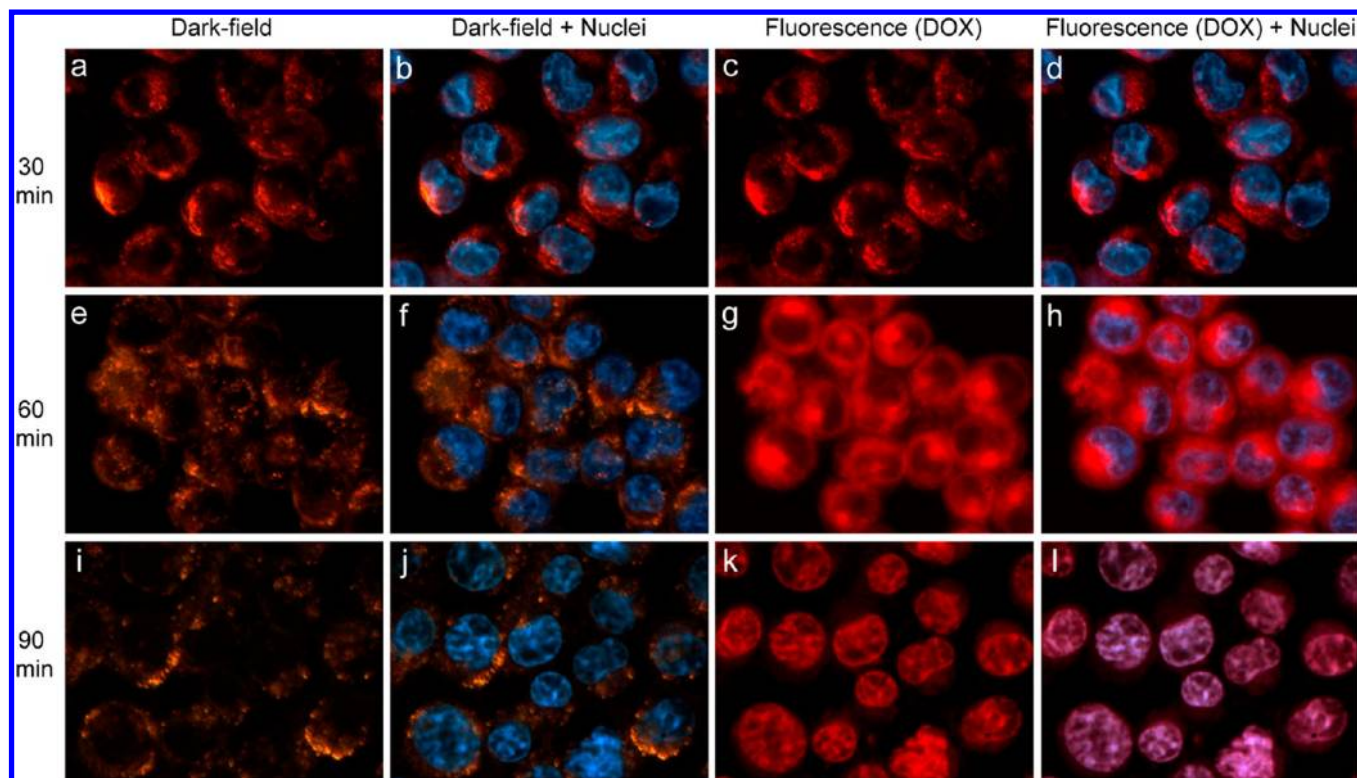


**Figure 9.** Dark-field (a, e, i), fluorescence (c, g, k), and the overlaid images (b, d, f, h, j, l) of SKBR-3 cells labeled with DOX-loaded pH-sensitive plasmonic vesicles after 30 min incubation (a–d) and the postincubation images of the cells at 60 min (e–h) and 90 min (i–l). DOX has a red fluorescence, and cell nuclei were counterstained with Hoechst 33342 exhibiting blue fluorescence.

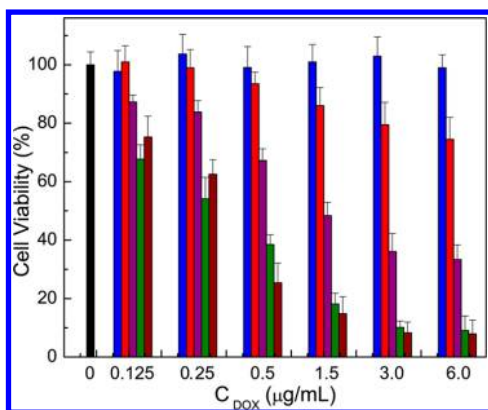


**Figure 10.** Cell viability data of targeted pH-sensitive vesicles with (green bar) and without (blue bar) DOX, nontargeted pH-sensitive vesicles with DOX (purple bar), targeted pH-insensitive vesicles with DOX (red bar), and free DOX (wine bar) obtained from cultured SKBR-3 cells (black bar: control SKBR-3 cells) using the CCK-8 assay.

envision that the plasmonic vesicles have considerable potential for targeted combination therapy by offering the possibility for cargo loading in both hydrophobic shell and aqueous cavity and integrating photothermal therapy<sup>25,40</sup> based on plasmonic nanostructures and chemotherapy of loaded therapeutic agents inside the vesicles. Additionally, the flexible synthesis of amphiphilic nanocrystals based on combined ligand exchange and surface-initiated polymerization also opens the opportunities toward plasmonic vesicles sensitive to a broad spectrum of biological stimuli such as oxidative stress<sup>42</sup> and glucose influx<sup>43</sup> for biosensing and localized therapy.

## EXPERIMENTAL SECTION

**Materials and Characterization.** Methyl methacrylate (MMA), 4-vinylpyridine (4VP), doxorubicin (DOX), copper(I) bromide (CuBr), *N,N,N',N',N''*-pentamethyldiethylenetriamine (PMDETA), and 1-ethyl-3,3-dimethylaminopropylcarbodiimide hydrochloride (EDAC) were purchased from Sigma-Aldrich. The monomers (MMA and 4VP) were first passed through a basic alumina column to remove inhibitors and then distilled over  $\text{CaH}_2$ . Methoxy-poly(ethylene glycol)-thiol (MPEG-SH) and carboxyl-poly(ethylene glycol)-thiol (HOOC-PEG-SH) with a molecular weight of 5 kDa were received from Laysan Bio, Inc. Hydrogen tetrachloroaurate(III) trihydrate ( $\text{HAuCl}_4 \cdot 3\text{H}_2\text{O}$ ) was from Alfa Aesar. 2,2'-Dithiobis[1-(2-bromo-2-methylpropionyloxy)ethane] (DTBE) was synthesized according to our previous report.<sup>44</sup> Raman dye 2-(4-(bis(4-(diethylamino)phenyl)(hydroxy)methyl)phenoxy)ethyl 5-(1,2-dithiolan-3-yl)pentanoate (BGLA) was synthesized following the method we reported recently.<sup>27b</sup> Hoechst 33342 used for cell nucleus staining was received from Life Technology.

Scanning electron microscopy (SEM) images were acquired on a FESEM (JSM-6700F). Transmission electron microscopy (TEM) observations were conducted on a JEOL JEM 2010 electron microscope at an acceleration voltage of 300 kV. UV-vis spectra were recorded using a Shimadzu UV2501 spectrophotometer. Fluorescence spectra were collected on a Fluoromax-3 spectrometer (Horiba Scientific). Hydrodynamic sizes were measured using a Malvern NANO-ZS90 Zetasizer. Imaging experiments were conducted on an Olympus IX71 inverted microscope with an oil-immersion dark-field condenser (NA 1.2), Photometrics CoolSNAP-cf cooled CCD, and a PIXIS:100B spectroscopy CCD. Plasmonic vesicles or live cells were immobilized on a polylysine-modified glass coverslip of a flow chamber for the imaging experiments.  $^1\text{H}$  NMR spectra were measured with a Bruker AV300, using  $\text{CDCl}_3$  as the solvent. Gel permeation chromatography (GPC) measurements were done on a Shimadzu HPLC system using chloroform as the eluent, and the molecular weight was calibrated with polystyrene standards. Thermogravimetric



analysis (TGA) was carried out on an SDT Q600 thermogravimetric analyzer. Samples were placed in platinum sample pans and heated under a nitrogen atmosphere at a rate of 10 °C/min to 100 °C and held for 30 min to completely remove residual solvent. Samples were then heated to 700 °C at a rate of 10 °C/min.

A RENISHAW Raman microscope with WIRE 2.0 software and 632.8 nm emission line of an air-cooled He–Ne laser was used for SERS measurements. The laser beam was focused by a 50X objective, and the laser power on samples was 0.45 mW with a laser spot size of 2–5 μm. A single scan with an integration time of 15 s was performed. The encoder feedback controlled the grating stage with a holographic grating of 1800 lines/mm on an interchangeable magnetic mount. Raman spectra of an aqueous dispersion of the vesicles and BGLA solution (30 mM in pH 3.0 DI water) were measured to determine the enhancement factor (EF) of SERS-encoded vesicles. EF was calculated using the equation  $EF = I_{\text{SERS}}N_{\text{normal}}/I_{\text{normal}}N_{\text{SERS}}$ , where  $I_{\text{SERS}}$  and  $I_{\text{normal}}$  are the peak intensity at 1615 cm<sup>-1</sup> of BGLA spectra obtained from the vesicles and the aqueous solution respectively, and  $N_{\text{SERS}}$  and  $N_{\text{normal}}$  are the corresponding number of BGLA molecules in the scattering volume (see Supporting Information for details).<sup>45</sup> A series of vesicle dispersions of different concentration in the range from 1.0 pM to 20 nM were measured, and a detection limit of 1.8 pM gold nanoparticles was found at a signal-to-noise (S/N) ratio of 3.

**Synthesis of Amphiphilic Polymer Brush Coated SERS-Active Gold Nanoparticles.** Citrate-stabilized gold nanoparticles 14 nm in size were first coated with the BGLA Raman reporter by adding 1 mL of BGLA DMF solution (0.1 mg/mL) into 80 mL of gold nanoparticle dispersion (3.3 nM) over 5 min, and the mixture was stirred for 15 min for sufficient loading of BGLA on gold nanoparticle surfaces. Afterward, the mixed polymer brushes of PEG and PMMVP were grown on the nanoparticles through sequentially conducted grafting to and grafting from reactions.<sup>19,27</sup> In the grafting to reaction, the solution of 50 mg of PEG (HOOC-PEG-SH and MPEG-SH with a molar ratio of 35:65) and 23 mg of DTBE in DMF was slowly added into the BGLA-coated gold nanoparticle dispersion. After 12 h, the nanoparticles were purified by repeated centrifugation (10 000g, 20 min) to remove free PEG and DTBE and were redispersed in DMF for further use. In the grafting from reaction, 300 mg of MMA and 4VP with a molar ratio of 9:1.5 and the functionalized nanoparticles (50 nM) were mixed in 2 mL of DMF. After the mixture was degassed by N<sub>2</sub>, CuBr (4 mg) and PMDETA (15 mg) were added to catalyze the polymerization. The reaction mixture was kept in a 50 °C water bath for 10 h and then centrifuged to remove unreacted monomers and the catalysts. The polymer-coated gold nanoparticles were stored in chloroform.

**Preparation of the Plasmonic Vesicles and the DOX-Loaded Vesicles and in Vitro Drug Release Study.** The amphiphilic gold nanoparticles were assembled into vesicles using the film rehydration method. Briefly, 0.15 mL dispersion (200 nM) of the gold nanoparticles in chloroform was first thoroughly dried on the wall of a glass vial under a steady flow of N<sub>2</sub> gas, and then 1 mL of DI water was added to rehydrate the film. DOX was deprotonated with equal molar of triethyl amine and dissolved in chloroform. To prepare DOX-loaded vesicles, 20 μL of chloroform solution of 150 μg of DOX was codeposited with the gold nanoparticle to form the film to be rehydrated with 1 mL of pH 7.4 PBS or 1 mL of pH 10 NaHCO<sub>3</sub> buffer. The as-prepared vesicles were centrifuged to remove free DOX and washed three times before being redispersed in pH 7.4 PBS for characterization and further uses. The release profiles of DOX from the plasmonic vesicle were investigated at 37 °C in pH 5.0 acetate buffer and pH 7.4 PBS. The amount of DOX released was separated from the vesicles by centrifugation and quantified from the calibration curves of DOX established by the absorbance at 485 nm.

**Conjugation of Monoclonal HER2 Antibody on the Vesicles.** EDAC (0.5 mg) was added into a mixture of the gold vesicle (0.2 nmol of gold nanoparticle) and the monoclonal HER2 antibody (400 μg), and the reaction was carried out at 4 °C overnight. After removing the unconjugated antibody by centrifugation, the bioconjugated vesicles were stored in pH 7.4 PBS at 4 °C before use.

**Cellular Studies.** SKBR-3 and MCF-7 cells were cultured in RPMI 1640 medium and DMEM medium supplemented with 10% fetal bovine serum and 1% antibiotics for 2–3 days (37 °C, 5% CO<sub>2</sub>) prior to the imaging experiments. To prepare live cells for imaging and spectroscopic detection, cells were seeded and allowed to adhere on polylysine-modified glass slides placed in a culture dish overnight. The bioconjugated vesicles or control samples (the final concentration of gold nanoparticle is 0.2 nM) in 2 mL of culture medium were incubated with the cells for 30 min. Afterward, cells were washed in PBS to remove free unbound samples, and fresh medium was added for imaging and spectroscopic detection at predetermined time intervals. To identify the intracellular location of the vesicles, the acidic organelles were stained with a green fluorescent dye, DIO, which was codelivered with the vesicles at a concentration of 2.0 μg/mL. To monitor the intracellular DOX release by combined dark-field and fluorescence imaging, cell nuclei of SKBR-3 cells were counterstained with Hoechst 33342 and treated with the DOX-loaded vesicles. The fluorescence signal of DOX was detected using wideband blue excitation (450–480 nm) provided by a mercury lamp, a long-pass dichroic filter (500 nm), and a band-pass emission filter (590–630 nm).

**Flow Cytometric Analyses of Cells.** Prior to analysis, SKBR-3 and MCF-7 cells were incubated with HER2 antibody and secondary antimouse antibody (Alexa Fluor 594 Goat Anti-Mouse IgG) sequentially. Both cell lines were treated with normal mouse IgG1 as controls. The BD FACS Calibur was utilized to perform flow cytometry, and FlowJo (Tree Star) was utilized to analyze the data.

**Cytotoxicity Assay.** Cytotoxicity of the plasmonic vesicles was evaluated using a standard cell-counting Kit-8 (CCK-8) assay.<sup>46</sup> The assay was carried out in triplicate in the following manner. SKBR-3 cells were seeded into 96-well plates at a density of 1 × 10<sup>4</sup> per well in 100 μL of media and grown overnight. The cells were then incubated with various concentrations of the vesicles and control samples. The concentrations of DOX were 0, 0.125, 0.25, 0.5, 1.5, 3.0, and 6.0 μg/mL. After incubation for 2 h, the medium was replaced with fresh medium, and the cells were maintained in the incubator for 24 h. To measure the cell viability, CCK-8 solutions were added to each tested wells and incubated for 4 h. Since the amount of formazan (produced from the cleavage of CCK-8 by dehydrogenase in live cells) was proportional to the number of live cells, the absorbance of each sample at 450 nm was measured using a microplate reader of all cells. The cell viability was calculated as the ratio of the absorbance of the sample well to that of the control wells and expressed as a percentage. Data presented are averaged results of triplicated experiments.

## ■ ASSOCIATED CONTENT

### § Supporting Information

Supporting figures including GPC, <sup>1</sup>H NMR, and TGA results of the amphiphilic gold nanoparticles. This material is available free of charge via the Internet at <http://pubs.acs.org>.

## ■ AUTHOR INFORMATION

### Corresponding Author

hduan@ntu.edu.sg

### Notes

The authors declare no competing financial interest.

## ■ ACKNOWLEDGMENTS

H.D. thanks the Nanyang Assistant Professorship for financial support. This work is supported in part by the INSIST program at Nanyang Technological University.

## ■ REFERENCES

- (1) (a) Jain, P. K.; Huang, X. H.; El-Sayed, I. H.; El-Sayed, M. A. *Acc. Chem. Res.* **2008**, *41*, 1578–1586. (b) Rosi, N. L.; Mirkin, C. A. *Chem. Rev.* **2005**, *105*, 1547–1562. (c) Halas, N. J. *Nano Lett.* **2010**, *10*, 3816–3822.



- (2) (a) Anker, J. N.; Hall, W. P.; Lyandres, O.; Shah, N. C.; Zhao, J.; Van Duyne, R. P. *Nat. Mater.* **2008**, *7*, 442–453. (b) Qian, X. M.; Nie, S. M. *Chem. Soc. Rev.* **2008**, *37*, 912–920. (c) Saha, K.; Agasti, S. S.; Kim, C.; Li, X.; Rotello, V. M. *Chem. Rev.* **2012**, *112*, 2739–2779.
- (3) (a) Tao, A. R.; Habas, S.; Yang, P. *Small* **2008**, *4*, 310–325. (b) Skrabalak, S. E.; Chen, J.; Sun, Y.; Lu, X.; Au, L.; Cobley, C. M.; Xia, Y. *Acc. Chem. Res.* **2008**, *41*, 1587–1595. (c) Mayer, K. M.; Hafner, J. H. *Chem. Rev.* **2011**, *111*, 3828–3857.
- (4) (a) Nie, Z.; Petukhova, A.; Kumacheva, E. *Nat. Nanotechnol.* **2010**, *5*, 15–25. (b) Tan, S. J.; Campolongo, M. J.; Luo, D.; Cheng, W. *Nat. Nanotechnol.* **2011**, *6*, 268–276. (c) Grzelczak, M.; Vermant, J.; Furst, S. M.; Liz-Marzán, L. M. *ACS Nano* **2010**, *4*, 3591–3605.
- (5) (a) Wang, Z. X.; Levy, R.; Fernig, D. G.; Brust, M. *J. Am. Chem. Soc.* **2006**, *128*, 2214–2215. (b) Kim, S.; Park, J. W.; Kim, D. K.; Kim, D. J.; L. I. H. Jon, S. Y. *Angew. Chem., Int. Ed.* **2009**, *48*, 4138–4141.
- (6) (a) Zhu, M. Q.; Wang, L. Q.; Exarhos, G. J.; Li, A. D. Q. *J. Am. Chem. Soc.* **2004**, *126*, 2656–2657. (b) Shen, Y.; Kuang, M.; Shen, Z.; Nieberle, J.; Duan, H. W.; Frey, H. *Angew. Chem., Int. Ed.* **2008**, *47*, 2227–2230.
- (7) Raschke, G.; Kowarik, S.; Franzl, T.; Sönnichsen, C.; Klar, T. A.; Feldmann, J.; Nichtl, A.; Kürzinger, K. *Nano Lett.* **2003**, *7*, 935–938.
- (8) (a) Sönnichsen, C.; Reinhard, B. M.; Liphardt, J.; Alivisatos, A. P. *Nat. Biotechnol.* **2005**, *23*, 741–745. (b) Reinhard, B. M.; Sheikholeslami, S.; Mastroianni, A.; Alivisatos, A. P.; Liphardt, J. *Proc. Natl. Acad. Sci. U. S. A.* **2007**, *104*, 2667–2672. (c) Jun, Y. W.; Sheikholeslami, S.; Hostetter, D. R.; Tajon, C.; Craik, C. S.; Alivisatos, A. P. *Proc. Natl. Acad. Sci. U. S. A.* **2009**, *106*, 17735–17740.
- (9) (a) Wang, J.; Boriskina, S. V.; Wang, H.; Reinhard, B. M. *ACS Nano* **2011**, *5*, 6619–6628. (b) Crow, M. J.; Seekell, K.; Ostrander, J. H.; Wax, A. *ACS Nano* **2011**, *5*, 8532–8540.
- (10) Alvarez-Puebla, R. A.; Liz-Marzán, L. M. *Small* **2010**, *6*, 604–610.
- (11) Camden, J. P.; Dieringer, J. A.; Zhao, J.; Van Duyne, R. P. *Acc. Chem. Res.* **2008**, *41*, 1653–1661.
- (12) (a) Chen, G.; Wang, Y.; Yang, M. X.; Xu, J.; Goh, S. J.; Pan, M.; Chen, H. Y. *J. Am. Chem. Soc.* **2010**, *132*, 3644–3645. (b) Wustholz, K. L.; Henry, A. I.; McMahon, J. M.; Freeman, R. G.; Valley, N.; Piotti, M. E.; Natan, M. J.; Schatz, G. C.; Van Duyne, R. P. *J. Am. Chem. Soc.* **2010**, *132*, 10903–10910.
- (13) (a) Graham, D.; Thompson, D. G.; Smith, W. E.; Faulds, K. *Nat. Nanotechnol.* **2008**, *3*, 548–551. (b) Qian, X. M.; Li, J.; Nie, S. M. *J. Am. Chem. Soc.* **2009**, *131*, 7540–7541. (c) Xu, L.; Kuang, H.; Xu, C.; Ma, W.; Wang, L.; Kotov, N. A. *J. Am. Chem. Soc.* **2012**, *134*, 1699–1709.
- (14) (a) Thakor, A. S.; Jokerst, J.; Zavaleta, C.; Massoud, T. F.; Gambhir, S. S. *Nano Lett.* **2011**, *11*, 4029–4036. (b) Rana, S.; Bajaj, A.; Mout, R.; Rotello, V. M. *Adv. Drug Delivery Rev.* **2012**, *64*, 200–216.
- (15) (a) Gibson, J. D.; Khanal, B. P.; Zubarev, E. R. *J. Am. Chem. Soc.* **2007**, *129*, 11653–11661. (b) You, J.; Zhang, G. D.; Li, C. *ACS Nano* **2010**, *4*, 1033–1041. (c) Wang, F.; Wang, Y.-C.; Dou, S.; Xiong, M.-H.; Sun, T.-M.; Wang, J. *ACS Nano* **2011**, *5*, 3679–3692. (d) Vigderman, L.; Manna, P.; Zubarev, E. R. *Angew. Chem., Int. Ed.* **2012**, *51*, 636–641.
- (16) (a) Yavuz, M. S.; Cheng, Y.; Chen, J.; Cobley, C. M.; Zhang, Q.; Rycenga, M.; Xie, J.; Kim, C.; Song, K. H.; Schwartz, A. G.; Wang, L. V.; Xia, Y. *Nat. Mater.* **2009**, *8*, 935–939. (b) Jin, Y. D.; Gao, X. H. *J. Am. Chem. Soc.* **2009**, *131*, 17774–17776. (c) Yang, X. C.; Samanta, B.; Agasti, S. S.; Jeong, Y.; Zhu, Z.-J.; Rana, S.; Miranda, O. R.; Rotello, V. M. *Angew. Chem., Int. Ed.* **2011**, *50*, 477–481. (d) Shim, M. S.; Kim, C. S.; Ahn, Y.-C.; Chen, Z.; Kwon, Y. J. *J. Am. Chem. Soc.* **2010**, *132*, 8316–8324. (e) Kim, C.; Agasti, S. S.; Zhu, Z.; Isaacs, L.; Rotello, V. M. *Nat. Chem.* **2010**, *2*, 962–966.
- (17) (a) Discher, D. E.; Eisenberg, A. *Science* **2002**, *297*, 967–973. (b) van Dongen, S. F. M.; de Hoog, H. P. M.; Peters, R. J. R. W.; Nallani, M.; Nolte, R. J. M.; van Hest, J. C. M. *Chem. Rev.* **2009**, *109*, 6212–6274. (c) Tanner, P.; Baumann, P.; Enea, R.; Onaca, O.; Palivan, C.; Meier, W. *Acc. Chem. Res.* **2011**, *44*, 1039–1049.
- (18) (a) Katz, J. S.; Zhong, S.; Ricart, B. G.; Pochan, D. J.; Hammer, D. A.; Burdick, J. A. *J. Am. Chem. Soc.* **2010**, *132*, 3654–3655.
- (b) Chen, R.; Pearce, D. J. G.; Fortuna, S.; Cheung, D. L.; Bon, S. A. F. *J. Am. Chem. Soc.* **2011**, *133*, 2151–2153. (c) Egli, S.; Nussbaumer, M. G.; Balasubramanian, V.; Chami, M.; Bruns, N.; Palivan, C.; Meier, W. *J. Am. Chem. Soc.* **2011**, *133*, 4476–4483. (d) Huang, J.; Bonduelle, C.; Thévenot, J.; Lecommandoux, S.; Heise, A. *J. Am. Chem. Soc.* **2012**, *134*, 119–122.
- (19) Song, J. B.; Cheng, L.; Liu, A. P.; Yin, J.; Kuang, M.; Duan, H. W. *J. Am. Chem. Soc.* **2011**, *133*, 10760–10763.
- (20) (a) Zubarev, E. R.; Xu, J.; Sayyad, A.; Gibson, J. D. *J. Am. Chem. Soc.* **2006**, *128*, 15098–15099. (b) Nie, Z. H.; Fava, D.; Kumacheva, E.; Zou, S.; Walker, G. C.; Rubinstein, M. *Nat. Mater.* **2007**, *6*, 609–614. (c) Cheng, L.; Song, J.; Yin, J.; Duan, H. *J. Phys. Chem. Lett.* **2011**, *2*, 2258–2262. (d) Hu, J.; Wu, T.; Zhang, G.; Liu, S. *J. Am. Chem. Soc.* **2012**, *134*, 7624–7627.
- (21) (a) Lee, J. E.; Lee, N.; Kim, T.; Kim, J.; Hyeon, T. *Acc. Chem. Res.* **2011**, *44*, 893–902. (b) Nyström, A. M.; Wooley, K. L. *Acc. Chem. Res.* **2011**, *44*, 969–978. (c) Jokerst, J. V.; Gambhir, S. S. *Acc. Chem. Res.* **2011**, *44*, 1050–1060. (d) Shi, J.; Xiao, Z.; Kamaly, N.; Farokhzad, O. C. *Acc. Chem. Res.* **2011**, *44*, 1123–1134.
- (22) (a) Bae, Y.; Fukushima, S.; Harada, A.; Kataoka, K. *Angew. Chem., Int. Ed.* **2003**, *42*, 4640–4643. (b) Lee, E. S.; Gao, Z. G.; Kim, D.; Park, K.; Kwon, I. C.; Bae, Y. H. *J. Controlled Release* **2008**, *129*, 228–236. (c) Su, J.; Chen, F.; Cryns, V. L.; Messersmith, P. B. *J. Am. Chem. Soc.* **2011**, *133*, 11850–11853. (d) Du, J. Z.; Du, X. J.; Mao, C. Q.; Wang, J. *J. Am. Chem. Soc.* **2011**, *133*, 17560–17563.
- (23) (a) Bagalkot, V.; Zhang, L.; Levy-Nissenbaum, E.; Jon, S.; Kantoff, P. W.; Langer, R. Farokhzad, O. C. *Nano Lett.* **2007**, *7*, 3065–3070. (b) Zheng, D.; Seferos, D. S.; Giljohann, D. A.; Patel, P. C.; Mirkin, C. A. *Nano Lett.* **2009**, *9*, 3258–3261. (c) Kim, C. K.; Ghosh, P.; Pagliuca, C.; Zhu, Z. J.; Menichetti, S.; Rotello, V. M. *J. Am. Chem. Soc.* **2009**, *131*, 1360–1361. (d) Huschka, R.; Zuloaga, J.; Knight, M. W.; Brown, L. V.; Nordlander, P.; Halas, N. J. *J. Am. Chem. Soc.* **2011**, *133*, 11247–11255.
- (24) Sapsford, K. E.; Berti, L.; Medintz, I. L. *Angew. Chem., Int. Ed.* **2006**, *45*, 4562–4588.
- (25) (a) Xia, Y.; Li, W.; Cobley, C. M.; Chen, J.; Xia, X.; Zhang, Q.; Yang, M.; Cho, E. C.; Brown, P. K. *Acc. Chem. Res.* **2011**, *44*, 914–924. (b) Bardhan, R.; Lal, S.; Joshi, A.; Halas, N. J. *Acc. Chem. Res.* **2011**, *44*, 936–946.
- (26) (a) Qian, X. M.; Peng, X. H.; Ansari, D. O.; Yin-Goen, Q.; Chen, G. Z.; Shin, D. M.; Yang, L.; Young, A. N.; Wang, M. D.; Nie, S. M. *Nat. Biotechnol.* **2008**, *26*, 83–90. (b) Keren, S.; Zavaleta, C.; Cheng, Z.; de la Zerda, A.; Gheysens, O.; Gambhir, S. S. *Proc. Natl. Acad. Sci. U. S. A.* **2008**, *105*, 5844–5849. (c) von Maltzahn, G.; Centrone, A.; Park, J. H.; Ramanathan, R.; Sailor, M. J.; Hatton, T. A.; Bhatia, S. N. *Adv. Mater.* **2009**, *21*, 3175–3180. (d) Lu, W.; Singh, A. K.; Khan, S. A.; Senapati, D.; Yu, H.; Ray, P. C. *J. Am. Chem. Soc.* **2010**, *132*, 18103–18114.
- (27) (a) Cheng, L.; Liu, A.; Peng, S.; Duan, H. *ACS Nano* **2010**, *4*, 6098–6104. (b) Yin, J.; Wu, T.; Song, J.; Zhang, Q.; Liu, S.; Xu, R.; Duan, H. W. *Chem. Mater.* **2011**, *23*, 4756–4764.
- (28) Prencipe, G.; Tabakman, S. M.; Welsher, K.; Liu, Z.; Goodwin, A. P.; Zhang, L.; Henry, J.; Dai, H. J. *J. Am. Chem. Soc.* **2009**, *131*, 4783–4787.
- (29) Kuang, M.; Wang, D. Y.; Bao, H. B.; Gao, M. Y.; Möhwald, H.; Jiang, M. *Adv. Mater.* **2005**, *17*, 267–270.
- (30) Casey, J. R.; Grinstein, S.; Orlowski, J. *Nat. Rev. Mol. Cell Biol.* **2010**, *11*, 50–61.
- (31) Krug, J. T., II; Wang, G. D.; Emory, S. R.; Nie, S. M. *J. Am. Chem. Soc.* **1999**, *121*, 9208–9214.
- (32) Discher, B. M.; Won, Y. Y.; Ege, D. S.; Lee, J. C. M.; Bates, F. S.; Discher, D. E.; Hammer, D. A. *Science* **1999**, *284*, 1143–1146.
- (33) (a) Mendelsohn, J.; Baselga, J. *Oncogene* **2000**, *19*, 6550–6565. (b) Wu, X. Y.; Liu, H. J.; Liu, J. Q.; Haley, K. N.; Treadway, J. A.; Larson, J. P.; Ge, N. F.; Peale, F.; Bruchez, M. P. *Nat. Biotechnol.* **2003**, *21*, 41–46.
- (34) Huang, H.; Groth, J.; Sossey-Alaoui, K.; Hawthorn, L.; Beall, S.; Geradts, J. *Clin. Cancer Res.* **2005**, *11*, 4357–4364.

- (35) (a) Derfus, A. M.; Chan, W. C. W.; Bhatia, S. N. *Adv. Mater.* **2004**, *16*, 961–966. (b) Duan, H. W.; Nie, S. M. *J. Am. Chem. Soc.* **2007**, *129*, 3333–3338. (c) Bayles, A. R.; Chahal, H. S.; Chahal, D. S.; Goldbeck, C. P.; Cohen, B. E.; Helms, B. A. *Nano Lett.* **2010**, *10*, 4086–4092.
- (36) (a) Han, J.; Burgess, K. *Chem. Rev.* **2010**, *110*, 2709–2728. (b) Zhou, K.; Wang, Y.; Huang, X.; Luby-Phelps, K.; Sumer, B. D.; Gao, J. *Angew. Chem., Int. Ed.* **2011**, *50*, 6109–6114.
- (37) (a) Bishnoi, S. W.; Rozell, C. J.; Levin, C. S.; Gheith, M. K.; Johnson, B. R.; Johnson, D. H.; Halas, N. J. *Nano Lett.* **2006**, *6*, 1687–1692. (b) Kneipp, J.; Kneipp, H.; McLaughlin, M.; Brown, D.; Kneipp, K. *Nano Lett.* **2006**, *6*, 2225–2231. (c) Pallaoro, A.; Braun, G. B.; Reich, N. O.; Moskovits, M. *Small* **2010**, *6*, 618–622.
- (38) (a) Mayer, L. D.; Bally, M. B.; Cullis, P. R. *Biochim. Biophys. Acta* **1986**, *857*, 123–126. (b) Choucair, A.; Soo, P. L.; Eisenberg, A. *Langmuir* **2005**, *21*, 9308–9313. (c) Ahmed, F.; Pakunlu, R. I.; Brannan, A.; Bates, F.; Minko, T.; Discher, D. E. *J. Controlled Release* **2006**, *116*, 150–158. (d) Lee, S. M.; Ahn, R. W.; Chen, F.; Fought, A. J.; O'Halloran, T. V.; Cryns, V. L.; Nguyen, S. T. *ACS Nano* **2010**, *4*, 4971–4978.
- (39) (a) Sanson, C.; Schatz, C.; Le Meins, J. F.; Soum, A.; Thevenot, J.; Garanger, E.; Lecommandoux, S. *J. Controlled Release* **2010**, *147*, 428–435. (b) Sanson, C.; Diou, O.; Thévenot, J.; Ibarboure, E.; Soum, A.; Brûlet, A.; Miraux, S.; Thiaudière, E.; Tan, S.; Brisson, A.; Dupuis, V.; Sandre, O.; Lecommandoux, S. *ACS Nano* **2011**, *5*, 1122–1140.
- (40) (a) Huang, X. H.; El-Sayed, I. H.; Qian, W.; El-Sayed, M. A. *J. Am. Chem. Soc.* **2006**, *128*, 2115–2120. (b) Chen, J. Y.; Wang, D. L.; Xi, J. F.; Au, L.; Siekkinen, A.; Warsen, A.; Li, Z. Y.; Zhang, H.; Xia, Y. N.; Li, X. D. *Nano Lett.* **2007**, *7*, 1318–1322. (c) von Maltzahn, G.; Park, J. H.; Agrawal, A.; Bandaru, N. K.; Das, S. K.; Sailor, M. J.; Bhatia, S. N. *Cancer Res.* **2009**, *69*, 3892–3900. (d) Fan, Z.; Shelton, M.; Singh, A. K.; Senapati, D.; Khan, S. A.; Ray, P. C. *ACS Nano* **2012**, *6*, 1065–1073.
- (41) Barbey, R.; Lavanant, L.; Paripovic, D.; Schtüwer, N.; Sugnaux, C.; Tugulu, S.; Klok, H. A. *Chem. Rev.* **2009**, *109*, 5437–5527.
- (42) Li, C.; Hu, J.; Liu, T.; Liu, S. *Macromolecules* **2011**, *44*, 429–431.
- (43) Matsumoto, A.; Ikeda, S.; Harada, A.; Kataoka, K. *Biomacromolecules* **2003**, *4*, 1410–1416.
- (44) Duan, H. W.; Wang, D. A.; Kurth, D. G.; Möhwald, H. *Angew. Chem., Int. Ed.* **2004**, *43*, 5639–5642.
- (45) (a) Wustholz, K. L.; Henry, A.; McMahon, J. M.; Freeman, R. G.; Valley, N.; Piotti, M. E.; Natan, M. J.; Schatz, G. C.; Van Duyne, R. P. *J. Am. Chem. Soc.* **2010**, *132*, 10903–10910. (b) Osberg, K. D.; Rycenga, M.; Harris, N.; Schmucker, A. L.; Langille, M. R.; Schatz, G. C.; Mirkin, C. A. *Nano Lett.* **2012**, *12*, 3828–3832.
- (46) Liu, A. P.; Peng, S.; Soo, J. C.; Kuang, M.; Chen, P.; Duan, H. W. *Anal. Chem.* **2011**, *83*, 1124–1130.

**Supporting Information for:**

**Self-Assembled Plasmonic Vesicles of SERS-Encoded  
Amphiphilic Gold Nanoparticles for Cancer Cell Targeting  
and Traceable Intracellular Drug Delivery**

*Jibin Song, Jiajing Zhou, Hongwei Duan\**

School of Chemical and Biomedical Engineering, Nanyang Technological University,  
70 Nanyang Drive, Singapore 637457

Email: hduan@ntu.edu.sg

**Calculation of the graft density of polymer brushes on Au nanoparticles.** Given the size of a gold atom ( $0.017\text{nm}^3$ ), the number of gold atom ( $N_{\text{Au atom}}$ ) in  $14\text{nm}$  Au nanoparticles can be calculated using Equation S1, where  $R$  is the radius of the gold nanoparticles. The result is 84472 gold atoms per nanoparticle and therefore the molar mass ( $M_{\text{Au nanoparticle}}$ ) of the gold nanoparticle is  $197N_{\text{Au atom}}$ . Combining the molar mass of the gold nanoparticle, the ratio of PEG and PMMA and the weight fraction obtained in TGA analysis, the average number of polymer grafts can be calculated by Equation S2, where  $W_{\text{polymer}}$  is the weight fraction (21%) of the organic part,  $W_{\text{Au nanoparticle}}$  is the weight fraction of gold nanoparticle and  $M_{\text{PEG+2PMMA}}$  is the sum of the molar mass of one PEG and two PMMA grafts. The result is 246 grafts per nanoparticle, which include 82 PEG chains and 164 PMMA chains, and the graft density is  $\sim 0.4$  chain/ $\text{nm}^2$ .

$$N_{\text{Au atom}} = \frac{V_{\text{Au nanoparticle}}}{V_{\text{Au atom}}} = \frac{4\pi}{3} \left( \frac{R^3}{V_{\text{Au atom}}} \right) \quad (\text{Equation S1})$$



$$N_{\text{grafts per nanoparticle}} = \left( \frac{3W_{\text{polymer}}/M_{\text{PEG+2PMMA}}}{W_{\text{Au nanoparticle}}/M_{\text{Au nanoparticle}}} \right) \quad (\text{Equation S2})$$

**Calculation of the ensemble-averaged enhancement factor (EF) of the SERS-active plasmonic vesicles.** EF was calculated using the equation,  $EF = (I_{\text{SERS}} \times N_{\text{normal}})/(I_{\text{normal}} \times N_{\text{SERS}})$ , where  $I_{\text{SERS}}$  and  $I_{\text{normal}}$  are the peak intensity at  $1615 \text{ cm}^{-1}$  of BGLA spectra obtained from the vesicles and the aqueous solution respectively, and  $N_{\text{SERS}}$  and  $N_{\text{normal}}$  are the corresponding number of BGLA molecules in the scattering volume.  $N_{\text{normal}}$  was calculated by the following equation,  $N_{\text{normal}} = C_{\text{normal}} \times V_{\text{scattering}}$ , where  $C_{\text{normal}}$  is the concentration of BGLA solution, and  $V_{\text{scattering}}$  is the scattering volume of the focused laser beam.  $N_{\text{SERS}}$  was estimated by the following equation,  $N_{\text{SERS}} = N \times C_{\text{Au NPs}} \times V_{\text{scattering}}$ , where  $N$  is the average number of BGLA on each 14 gold nanoparticles,  $C_{\text{Au NPs}}$  is the concentration of 14 nm gold nanoparticles in the vesicles dispersion, and  $V_{\text{scattering}}$  is the scattering volume of the focused laser beam. As a result, EF can be calculated by the following equation,  $EF = (I_{\text{SERS}} \times C_{\text{normal}})/(I_{\text{normal}} \times N \times C_{\text{Au NPs}})$ .

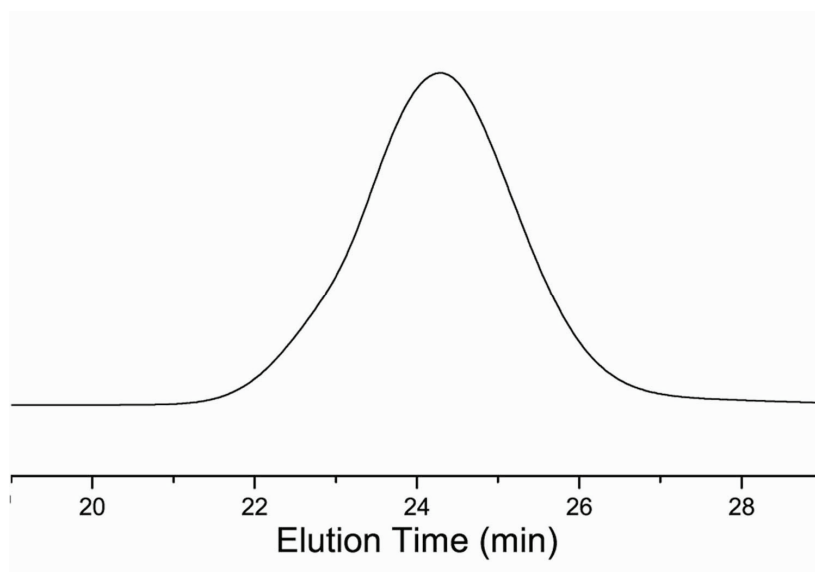


**Figure S1.** GPC trace of the copolymer of methyl methacrylate (MMA) and 4-vinyl pyridine (4VP) detached from the gold nanoparticles ( $M_n=24$  kDa, PDI=1.21).

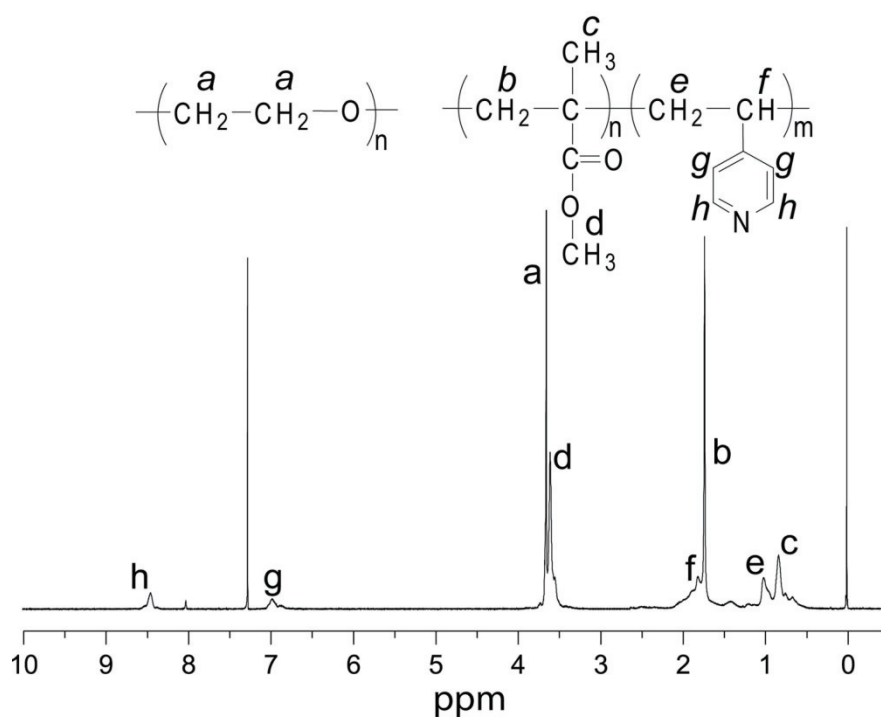


**Figure S2.**  $^1\text{H}$  NMR (300 MHz,  $\delta$ , ppm,  $\text{CDCl}_3$ ) of the amphiphilic gold nanoparticles coated with mixed polymer brushes of poly(ethylene glycol) and copolymer of methyl methacrylate (MMA) and 4-vinyl pyridine (4VP): 8.46 and 6.91 (*pyridine*), 3.67 ( $-\text{OCH}_2\text{CH}_2-$ ), 3.62 ( $-\text{OCH}_3$ ), 2.25 ( $-\text{CH}$ ), 1.24-2.16 ( $-\text{CH}_2$ ), 1.26 ( $-\text{CH}_2$ ), 0.36-1.27 ( $-\text{CH}_3$ ). The ratio of MMA and 4VP in the copolymer was calculated based on the resonance of pyridine (8.45 ppm) and that of  $-\text{CH}_3$  group (0.36-1.27 ppm) of MMA, leading to 10% of 4VP in the copolymer.



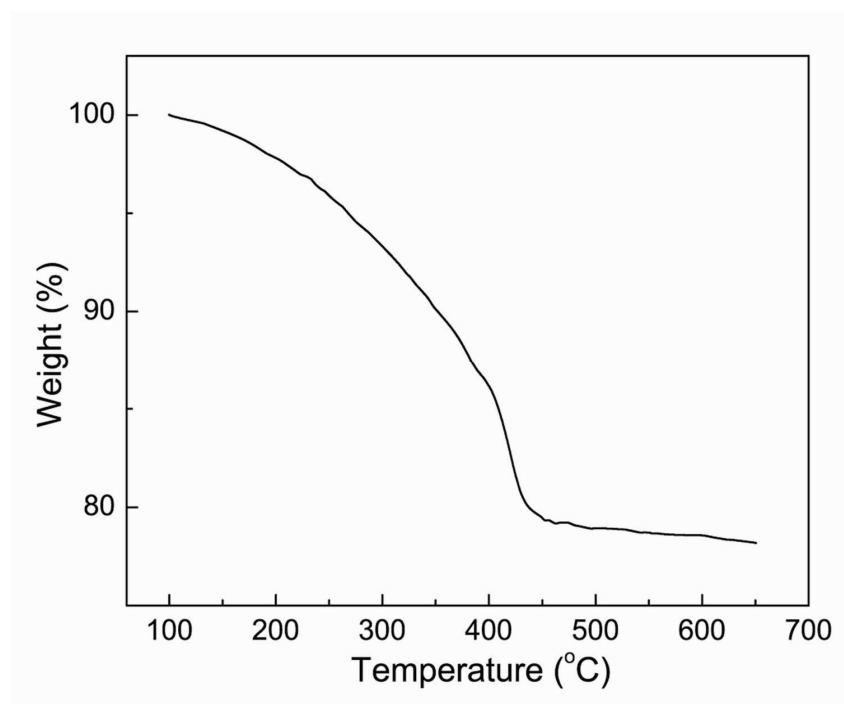


**Figure S3.** TGA analysis of the gold nanoparticles grafted with mixed polymer brushes of poly(ethylene glycol) and copolymer of methyl methacrylate (MMA) and 4-vinyl pyridine (4VP) (the weight fraction of the polymer brushes is 21%).

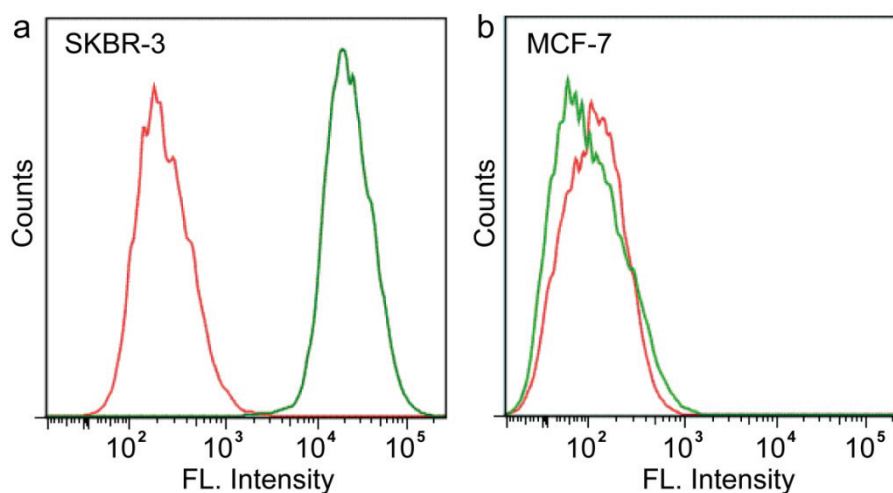


**Figure S4.** The flow cytometric analyses of SKBR-3 (a) and MCF-7 (b) cells labelled with a HER2 antibody and an Alexa Fluor® 594-conjugated secondary anti-mouse antibody (green line) and control cells (red line) incubated with normal mouse IgG1.

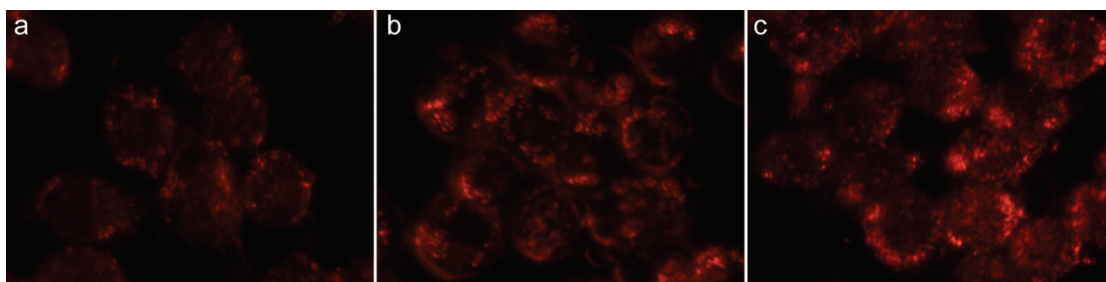


**Figure S5.** Dark-field images of SKBR-3 cells incubated with targeted vesicles for 10, 30, and 90 min.

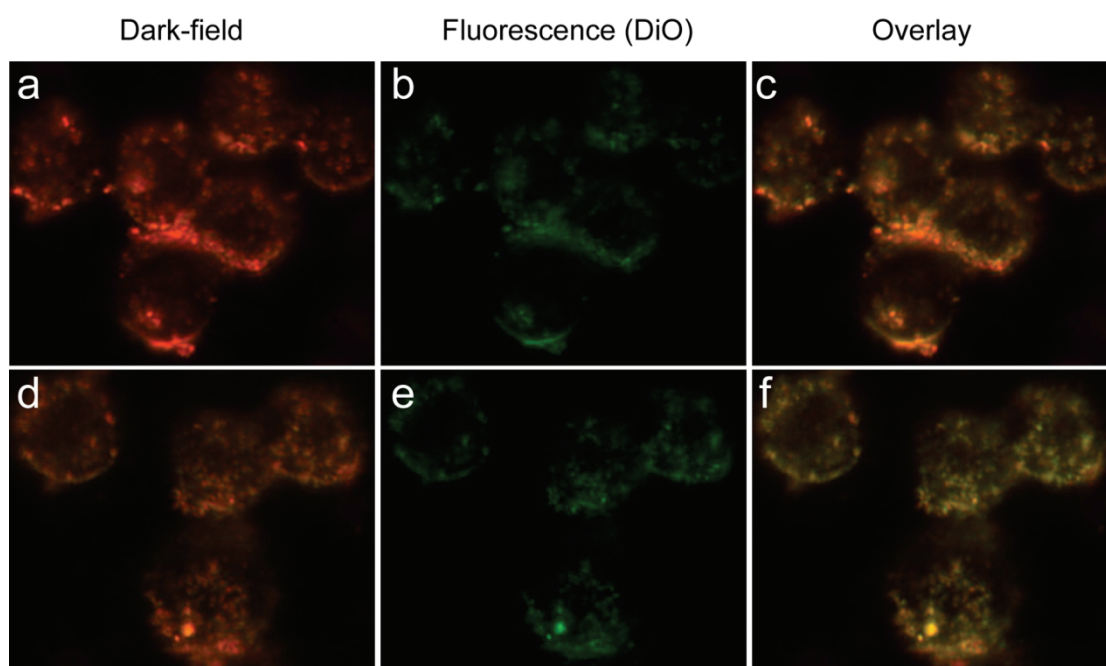


**Figure S6.** The co-localization of the plasmonic vesicles and the organelle-tracking dye DiO in SKBR-3 cells incubated with targeted vesicles for 30 min (a-c) and 60 min post-incubation (d-f).

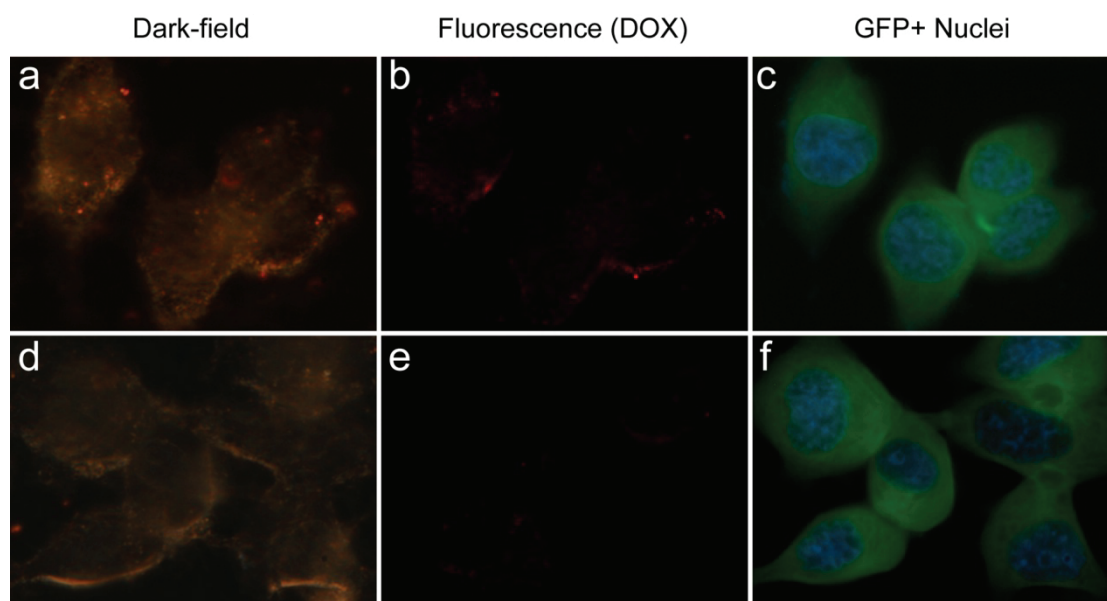


**Figure S7.** Dark-field (a, d), fluorescence (b, e), and the overlaid GFP and DAPI images (c, f) of MCF-7 cells labeled with DOX-loaded pH-sensitive plasmonic vesicle after incubated with targeted vesicles for 30 min (a-c) and 60 min post-incubation (d-f).